

A fully-coupled hydrological–mechanical–chemical model for fracture sealing and preferential opening

Jishan Liu^{a,*}, Jinchang Sheng^a, A. Polak^b, D. Elsworth^c, H. Yasuhara^c, A. Grader^c

^a*School of Oil & Gas Engineering, The University of Western Australia, 39 Stirling Highway, Crawley, WA 6009, Australia*

^b*Department of Civil and Environmental Engineering, Technion, Israel Institute of Technology, Haifa 32000, Israel*

^c*Energy Institute and Department of Energy and Geo-Environmental Engineering, Pennsylvania State University, University Park, PA 16802, USA*

Accepted 3 April 2005

Available online 23 June 2005

Abstract

A fully coupled hydrological–mechanical–chemical (HMC) model is developed and applied to explain enigmatic spontaneous changes in permeability that develop within a fracture in limestone under simulated in situ conditions (Water Resour Res 2004;40:W03502). The water flow-through test was concurrently monitored for water and dissolved mineral mass efflux and periodically imaged by X-ray CT to provide redundant constraints on fracture evolution by dissolution and precipitation. The resulting data, exhibiting a spontaneous switch between permeability-decreasing, and permeability-increasing, are evaluated using the HMC model. This model represents these two distinct behaviors: apertures first reduce, under presumed net dissolution, and then preferentially open as net dissolution is even more positively apparent. In the model, dissolution mechanisms within the fracture can be switched from mixed-mode (a combination of pressure dissolution and free-face dissolution) to single mode (pressure dissolution or free-face dissolution). This allows both permeability reduction as mineral mass is net removed from contacting asperities, and permeability enhancement as free-face dissolution localizes along a solution channel, to be accommodated and quantified. The model successfully replicates experimental measurements in limestone.

© 2005 Elsevier Ltd. All rights reserved.

Keywords: Permeability; Pressure dissolution; Free-face dissolution; Preferential flow; Numerical model

1. Introduction

Dissolution and precipitation of minerals on fracture walls modifies the permeability of a fracture either through sealing as contacting asperities are dissolved or through opening as fracture voids are etched by net dissolution. Sealing was reported for sandstone [1] and for granite [2] under high effective stress at elevated temperature (> 300 °C), for tuff at modest temperature (50–150 °C) [3] and for novaculite [4] at ambient temperatures. Sealing was also reported under low effective stress (0.2 MPa) with an acidic solution [5].

Conversely, opening was reported in carbonate reservoirs [6], and in the development of karst [7]. A recent study [8] demonstrated that these two opposing behaviors switch spontaneously without an apparent trigger. A number of previous studies reveal that fracture sealing is due to pressure dissolution at contact asperities whereas fracture opening is due to free-face dissolution at fracture voids. According to the concept of pressure dissolution, a stressed portion of a solid is more dissolvable than an unstressed portion [9]. Therefore, fracture-contacting asperities (similar to grain-to-grain contacts) were always dissolved in the initial stage [8,10–16]. As pressure dissolution progressed, the rate of dissolution decreased because stresses at those locations were lowered. When the stress reached a certain threshold, free-face dissolution at fracture void surfaces took

*Corresponding author. Tel.: +61 8 6488 7205;
fax: +61 8 6488 1964.

E-mail address: jishan@cyllene.uwa.edu.au (J. Liu).

place [9,17–19]. The free-face dissolution reduced the contact area further. Subsequently, the free-face dissolution at the periphery of contacts was followed by asperity crushing, as Weyl [11] suggested. Apparently, both pressure dissolution at contacting asperities and free-face dissolution at fracture void surfaces contribute to fracture sealing or opening. The focus of this work is to evaluate the relative importance of their contributions at different dissolution stages through an integrated approach of X-ray CT characterization for dissolution-modified flow paths and coupled hydrological–mechanical–chemical (HMC) simulations.

Flow paths within fractures are dynamic and evolve with time during dissolution. An important factor limiting our understanding of this phenomenon is the lack of information about the evolution of flow paths under in situ hydrological, chemical and mechanical conditions. A number of studies have observed that the dissolution/precipitation-induced evolution of flow paths can lead to preferential flow [20–26], and that macro-pore and preferential flow are important mechanisms for accelerated breakthroughs of tracers [27,28]. These rapid flow and transport processes reduce the potential for chemical degradation, retardation, and attenuation within geological media, therefore increasing the risk of chemical transport from its sources into groundwater [29,30]. To fully understand these important mechanisms, it is becoming increasingly clear that the accurate characterization of flow paths and their incorporation into flow simulations are needed. Recent applications of X-ray computed tomography (CT) techniques [4,31,32] have made it possible to achieve this goal. The usefulness of this technique in geological and geotechnical research has been demonstrated by many studies. The X-ray CT technique has been applied to measure fracture geometry [33]; to characterize coal [34]; to study waterflooding in low permeable chalk [35]; to investigate tracer diffusion from fractures into the

surrounding rock matrix [4,36,37]; to conduct analyses of geological processes such as the texture of igneous and metamorphic rocks [38]; to characterize and determine distributions of saturation, porosity and permeability [34,39,40]; to investigate particulate interactions within opencast coal mine backfills [30]; to determine contact areas in rock joints [41]; and to characterize gas adsorption and transport in coal seams [42,43]. In recent applications, Hirono et al. [44] applied the X-ray CT technique to visualize in situ fluid flow within deformed rock during permeability testing under atmospheric pressure. These applications demonstrate the utility of X-ray CT in the characterization of both geologic media and processes. In this study, X-ray CT imaging is used to characterize the evolution of dissolution-dependent flow paths under in situ stress conditions. With the constraint available from these characterizations, a fully coupled HMC diagnostic model is developed to represent fracture sealing and preferential opening within a limestone fracture.

2. Flow-through experiment

A flow-through test was completed on an artificial fracture in limestone at room temperature under ambient confining stress of 3.5 MPa. Detailed description of the experiment and experimental results are reported in a companion paper [8]. In this section, only a brief description of the experiment and the important experimental findings are reported in order to establish the basis for the subsequent numerical simulation.

2.1. Experiment description

A cylindrical sample (5 cm diameter \times 10.8 cm length) of Bellefonte Limestone, with a through-going axial fracture as shown in Fig. 1, was used to conduct the

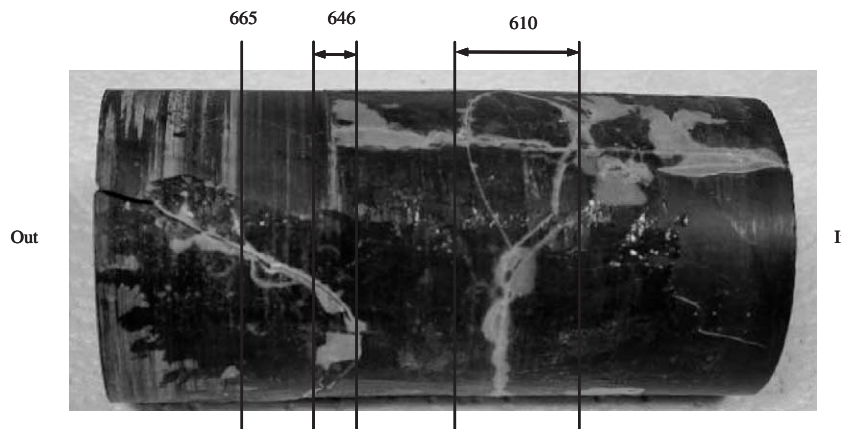


Fig. 1. The cylindrical core (5 cm in diameter and 10.8 cm in length) of Bellefonte Limestone. The core contains a diametrical fracture intersecting an axial fracture. Water is injected into the core from the right end and flows out from the left end. Numbers are used to indicate the scanning locations.

flow-through test. The core contains a diametrical fracture intersecting an axial fracture. The sample was fractured artificially using a modified Brazilian test. The experimental system includes a multi-phase fluid flow system, a core holder assembly that controls confining pressure, and an X-ray CT imaging system. A schematic of the system is shown in Fig. 2. The imaging system consists of an ionized X-ray source, a detector, a translation system, and a computer system that controls motions and data acquisition. The X-ray source has a Tungsten target with a focal spot of $5\ \mu\text{m}$. It produces a cone beam that passes through the core and activates the detector. The image intensifier detector surface releases electrons that are then focused on a screen that is photographed by a high-resolution (1024×1024) camera with a frequency of 15 Hz. The sample is rotated 360° in the X-ray beam while the detector provides attenuation views to the data acquisition computer. After the sample is rotated a complete turn, the system reconstructs a slice, a cross-sectional image of the attenuation values that represents a combination of the density and the apparent atomic number of the sample and the imaged position. The imager operates in volume mode where several separate slices are collected in one rotation. Fluids are introduced to the sample through pipes that are able to sustain the rotation and the translation of the sample. They were disconnected before scanning. There are two fluid injection lines, one

fluid production line, one confining pressure line, and two pressure measurement lines. In this study, we apply the imaging system to characterize the evolution of flow paths during reactive flow in an artificial limestone fracture.

X-ray imaging of two-dimensional slices perpendicular to the core axis was completed with a slice thickness of $50\ \mu\text{m}$ and an in-plane pixel resolution of $47\ \mu\text{m}$. The X-ray energy level used in the experiment was 195 kV at $800\ \mu\text{A}$. The sample and pressure vessel were removed from the CT scanner after each scan sequence. In order to ensure proper registration of the CT images two small ($1 \times 1 \times 1\ \text{mm}$) stainless steel targets were inserted into the outer flank of the fracture to act as fiducial marks. Following core packing, a total of four scans were taken at different stages of the experiment. The first scan was carried out after saturation to determine whether the fracture was completely open throughout its length and to serve as a baseline for the rest of the experiment. Three scans followed at an effective stress of 3.5 MPa, and represented progress of the experiment at 938, 1173, and 1492 h from the start of the experiment. These scans were conducted at those specific times when contrast changes of the differential pressure took place. Each scan sampled volumes at 3 different axial locations in the core (610, 646, and 665 representing distances of 30, 66 and 85 mm from the core's inlet, respectively). The first location (610) had 9 rotations each of 41 slices, representing an axial length of 18.45 mm ($50\ \mu\text{m}$ for each slice). The second location (646) had 3 rotations each of 41 slices, representing an axial length of 6.15 mm, and the third location a single rotation with an axial length of 2.05 mm.

2.2. Differential pressure

Tests were monitored for changes in differential pressure between the inlet and outlet and for mineral mass loss or gain and throughout the 1500 h duration of the experiment. Periodic imaging by X-ray CT augments the fluid and mineral mass balance data and provides a third independent constraint on dissolution processes. The sample was sequentially circulated by water of two different compositions through the 1500 h duration of the experiment; the first 932 h by sampled groundwater (pH \sim 8), followed by 555 h of distilled water (pH \sim 6). The evolution of the differential pressure with time is shown in Fig. 3. Large changes in the differential pressure were recorded throughout the experiment for the constant flow-rate of $2\ \text{cc m}^{-1}$; these were used as a proxy for recorded changes in fracture permeability, under invariant effective stress conditions. Mass of Ca and Mg were net-removed throughout the experiment. During the initial circulation of groundwater, the differential pressure increased almost threefold, and is interpreted as a net reduction in permeability as the

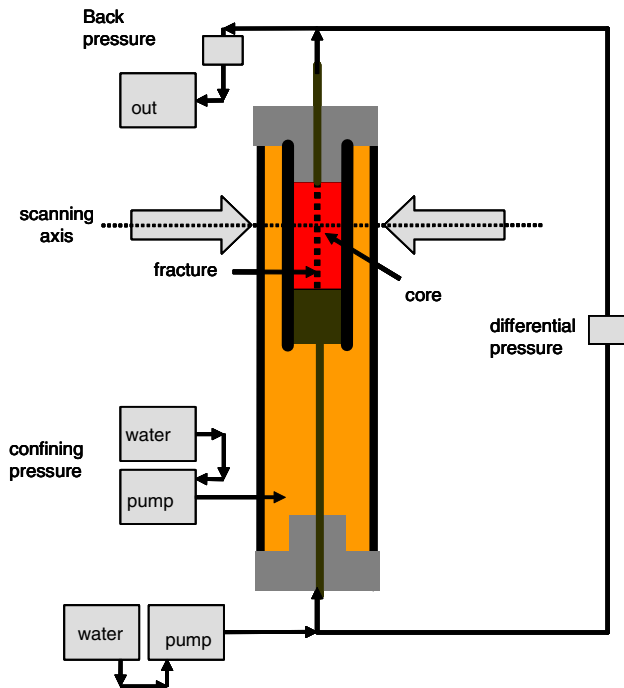


Fig. 2. A schematic diagram of the experimental setup. System comprises the fluid flow system, a core holder assembly that can provide controlled confining pressures, and an X-ray computed tomography system.

contacting asperities across the fracture are removed, and the fracture closes. With the circulation of distilled water, permeability initially reduced threefold, and ultimately increased by two orders of magnitude as a preferential flow path developed in the sample, and the test was terminated.

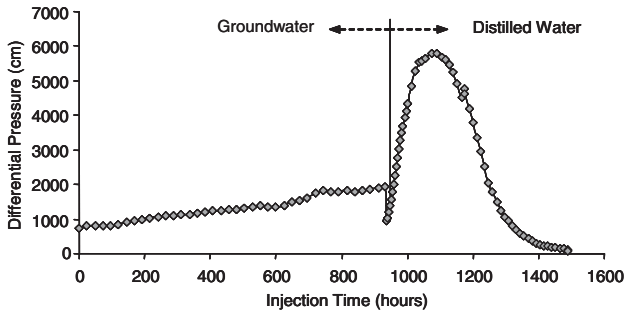


Fig. 3. Changes of differential pressure, in cm of water, with circulation time for a prescribed flux of $2\text{ cm}^3\text{ min}^{-1}$. Two distinct regions are observed: Differential pressure increases with until $t\sim 1088\text{ h}$, and falls exponentially following this. Pressure drop is taken as a proxy for changes in impedance within the fracture.

2.3. X-ray CT images

The formation of a preferential flow path was observed through X-ray CT images as shown in Fig. 4. Results of the first and fourth scanning sequences (0 and 1492 h, respectively) and at two different scanning locations (610 and 665) are shown in Fig. 4. Two vertical fractures and one horizontal fracture are visible in Fig. 4, which shows two scanning sequences at scanning position 610 that is situated 30 mm downstream from the core inlet. The two vertical fractures have a large aperture that is registered by the wide black signature. These fractures are not hydraulically connected and extend only for a few millimeters out-of-section, as measured by adjacent scans. No distinct difference evolves in these fractures between the two scanning sequences (as confirmed by the enlargement), as the water inside these fractures is stagnant during the experiment and the flow occurs only within the horizontal fracture. At location 665, 85 mm downstream of the inlet, the changes between the two sequences are visible at the area of the fracture where the wormhole develops. Two horizontal fractures are visible; the bottom fracture did not flow, as it was a local fracture.

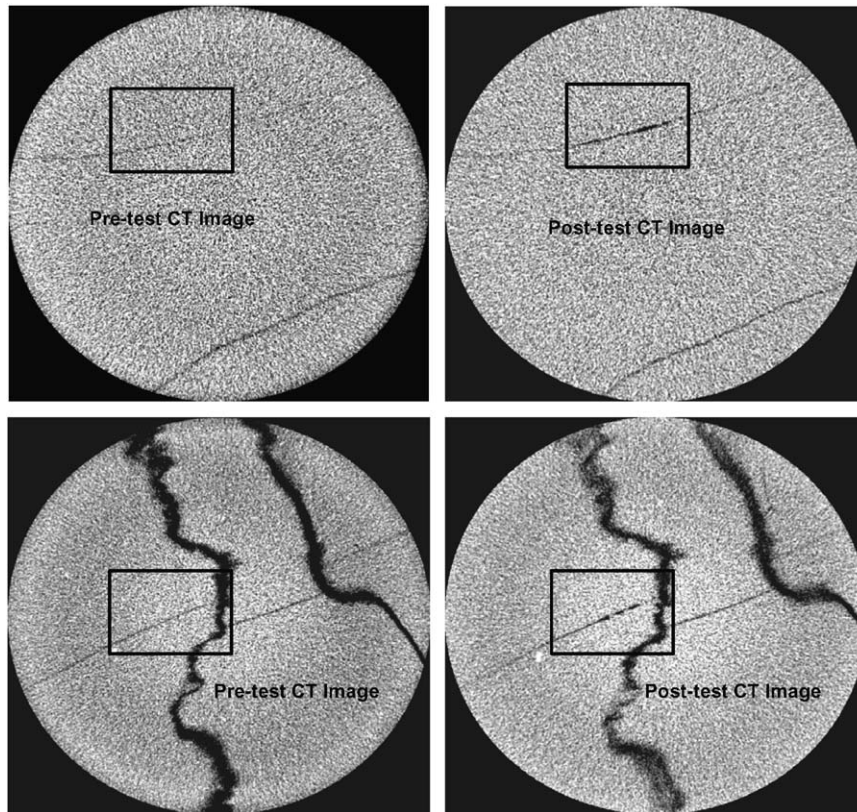


Fig. 4. Images of the Bellefonte Limestone Core Sample. These images are the scanning results of the first and the fourth scanning sequences (0 and 1492 h, respectively) at locations 665 (upper ones) and 610 (lower ones), which are 85 mm and 30 mm downstream from the core inlet, respectively. The changes are visible between these two sequences in the area of the fracture where preferential dissolution paths were formed. The two vertical fractures have large apertures apparent in the wide black signatures, but they are not hydraulically connected.

The primary flow is in the upper fracture, although at the current resolution of the CT system of 47 μm, no changes are apparent between the two sequences, except at the wormhole. The enlargement on the left side shows that even in the first scanning sequence the fracture appears closed, probably because the fracture aperture is smaller than the resolution of the system.

3. Model development

This spontaneous switch from net decrease in permeability, to net increase, occurred with no change in experimental conditions of flow-rate or applied effective stress, and Ca was net dissolved throughout. As revealed by the X-ray CT images, this behavior is attributed to the evolving localization of mass removal, triggered as free-face dissolution at fracture void surfaces out-competes pressure dissolution at the asperity contacts. A fully coupled HMC model is developed in the following, and applied to evaluate those experimental observations. These results are reported in the following sections.

3.1. Dissolution at contact areas

The important impact of dissolution at grain contacts on the deformation of sedimentary rocks has been recognized for many years [9,10,45]. Yasuhara et al. [46,47] defined the dissolution mass flux, dM_{diss}/dt , at grain-to-grain contacts as

$$\frac{dM_{\text{diss}}}{dt} = \frac{3\pi V_m^2 (\sigma_a - \sigma_c) k_+ \rho_g d_c^2}{4RT} = \alpha_0 (\sigma_a - \sigma_c), \quad (1)$$

where V_m is molar volume of the solid, σ_a is the disjoining pressure [45] equal to the amount by which the pressure acting at grain-to-grain contacts exceeds the hydrostatic pore pressure, σ_c is the critical stress, k_+ is the dissolution rate constant of the dissolved mineral, ρ_g is the grain density, d_c is the diameter of the grain-to-grain contacts, R is the gas constant, T is the temperature of the system, and α_0 is constant. The linear relation between dissolution mass flux and normal stress, as shown in Eq. (1), is valid only for grain-to-grain contacts, and may not be directly applicable to fractures with rock bridges as contact areas. Several experimental results [14,18] demonstrated a non-linear relation between the dissolution mass flux and normal stress for fractures. For example, Tada and Siever [18] and Gratier et al. [14] shown that the dissolution rate was low under low stress situation, and increased rapidly when effective normal stress exceeded 10–15 MPa. They postulated that the possible reason for the phenomena was that the contact areas were cracked or fractured by stresses. In this study, Eq. (1) is revised,

to incorporate the non-linearity for fractures, as

$$\frac{dG_a}{dt} = \alpha (\sigma_{\text{eff}} - \sigma_c)^\beta, \quad (2)$$

where G_a , as shown in Fig. 5, is the change in width due to dissolution at the contact area (rock bridge) in μm, α and β are constants, and σ_{eff} is the average effective stress at the contact area in MPa. β is a measure of the micro-cracking at asperity contacts. The impact of β on the dissolution rate is illustrated in Fig. 5. Three possible cases are discussed as follows:

- When $\beta > 1$, pressure dissolution rate is very low initially. As the effective stress increases gradually, the pressure solution rate increases moderately. When the effective stress becomes large enough to produce micro-cracks at the contact areas, the pressure dissolution rate increases dramatically as shown in Tada and Siever [18] and Gratier et al. [14].
- When $\beta = 1$, the relation between dissolution rate and effective stress becomes linear. This is the case that there are no micro-cracking regions at contact areas.
- When $\beta < 1$, this represents the unloading case where the ambient stress is initially applied, and only later fluid is circulated through the fracture. In this situation, the pressure dissolution rate is high at the beginning because the initial loading (ambient stress) may have caused regions of micro-cracking at the contact areas. As the removal process of asperities progresses, the pressure dissolution rate decreases because of the increase of the contact area and the subsequent decrease of the effective stress. When the micro-cracked regions at contact areas are removed completely, the pressure dissolution rate will return to the linear case.

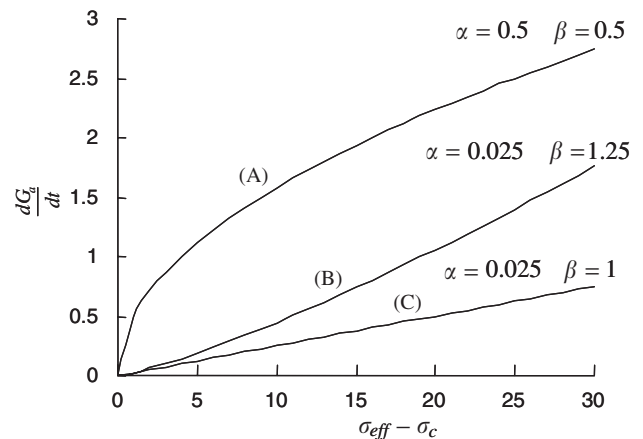


Fig. 5. Relations between the change of width at contact areas and the stress difference with different magnitudes of α and β : A—unloading case where micro-fracturing regions at contact areas are formed at the beginning of pressure dissolution; B—loading case where micro-cracking regions are formed during pressure dissolution; and C—grain-to-grain contact case where no micro-fracturing regions are formed.

3.2. Free-face dissolution

The mass flux, $dM_{\text{diss}}^{\text{FF}}/dt$, due to free-face dissolution, was defined [46], (Yasuhara et al. [46], modified from Palmer [7]; Dreybrodt and Buhmann [48]) as

$$\frac{dM_{\text{diss}}^{\text{FF}}}{dt} = k_+ A_{\text{pore}} \rho_g V_m \left(1 - \frac{C_{\text{pore}}}{C_{\text{eq}}}\right)^n, \quad (3)$$

where A_{pore} is the area of the fracture void, C_{pore} is the mass concentration in the pore fluid, C_{eq} is the equilibrium solubility of the dissolved mineral, and n is the reaction order. Dreybrodt [49] shown that the reaction kinetics was roughly first order for a pore fluid undersaturated with calcium, and the reaction order increased as the water approached the saturation. In this study, the order is assumed as unity. The dissolution mass flux will be zero when the mass concentration in the pore fluid is equal to the equilibrium solubility. Using $A_{\text{pore}} \rho_g$ to divide both sides of Eq. (3) yields

$$\frac{dG_f}{dt} = k_+ V_m \left(1 - \frac{C_{\text{pore}}}{C_{\text{eq}}}\right)^n, \quad (4)$$

where $G_f = M_{\text{diss}}^{\text{FF}}/(A_{\text{pore}} \rho_g)$ defines the retreat rate of the fracture wall due to free-face dissolution. If the mass concentration in the pore fluid, C_{pore} , is very low, it has no significant influence on the retreat rate [18]. Under this condition, the retreat-rate of the fracture wall is a constant. Assuming this constant as γ , Eq. (4) becomes

$$\frac{dG_f}{dt} = \gamma, \quad (5)$$

where $\gamma = k_+ V_m$.

3.3. Geometrical model

It is assumed that the rock fracture can be represented as a series of pores separated by contact areas, as illustrated in Fig. 6(a). The fracture profile is characterized through four geometrical parameters: the height of a pore, h_f , the angle of inclination of the pore wall, θ , the horizontal length of the pore, l_f , and the horizontal length of the contact area that separates adjacent pores, l_c . Although these parameters, or their statistical distribution, may be defined for a given fracture, their magnitude will evolve as dissolution proceeds both at asperity contacts and at pore surfaces. The evolution of the pore surfaces can be defined by the change in width due to dissolution at the contact area (rock bridge), G_a , and by the change in width due to dissolution at the pore surface, G_f . G_a and G_f are defined by Eqs. (2) and (4), respectively. Assuming that mass removal is uniform over the pore surface, the pore wall inclination will remain constant, at angle, θ . Under this assumption, the dissolution-dependent growth of pore height can be defined by Δh_f and Δl_c , as illustrated in Figs. 6(b) through (c). Changes in pore height and wall retreat are

related as

$$\Delta h_f = G_a - \frac{G_f}{\cos \theta}, \quad (6)$$

$$\Delta l_c = \frac{G_a}{\tan \theta} - \frac{G_f}{\sin \theta}. \quad (7)$$

During dissolution, the size of a pore could increase, decrease or remain unchanged depending on the values of Δh_f and Δl_c , dependent on the source of dissolution—at the pore walls or over the intervening asperity bridge.

3.3.1. Free-face dissolution

For free-face dissolution, substituting $G_a = 0$ into Eqs. (6) and (7) gives

$$\Delta h_f = -\frac{G_f}{\cos \theta}, \quad (8)$$

$$\Delta l_c = -\frac{G_f}{\sin \theta}. \quad (9)$$

It is apparent that both Δh_f and Δl_c are less than zero, indicating that the pore size increases with free-face dissolution.

3.3.2. Pressure dissolution

For pressure dissolution, substituting $G_f = 0$ into Eqs. (6) and (7) gives

$$\Delta h_f = G_a, \quad (10)$$

$$\Delta l_c = \frac{G_a}{\tan \theta}. \quad (11)$$

It is apparent that both Δh_f and Δl_c are greater than zero, indicating that the pore size decreases with pressure dissolution.

3.3.3. Mixed dissolutions

For most cases, dissolution is a combination of both free-face dissolution and pressure dissolution, i.e., $G_a \neq 0$, and $G_f \neq 0$. Under these circumstances, whether the pore size increases, decreases or remains unchanged will depend on the values of Δh_f and Δl_c . If $\Delta h_f = 0$ and $\Delta l_c = 0$, i.e., $G_a = G_f/\cos \theta$, the pore size will remain unchanged but the pore location may be changed. This phenomenon is called fracture transitioning. If $\Delta h_f < 0$ and $\Delta l_c < 0$, i.e., $G_a < (G_f/\cos \theta)$, the pore size will increase. In this study, the increase in the size of a pore defines ‘fracture opening’. Owing to the non-uniform distribution of pore sizes, fractures may open preferentially in different locations. This phenomenon results if $\Delta h_f > 0$ and $\Delta l_c > 0$, i.e., $G_a > (G_f/\cos \theta)$, then the pore size will decrease, and may ultimately seal. Again, sealing may occur preferentially, as driven by the initial non-uniform distribution of pore or fracture geometry. These terms (fracture transitioning, opening, and sealing) are used to represent how a flow path evolves during dissolution. For the case of fracture

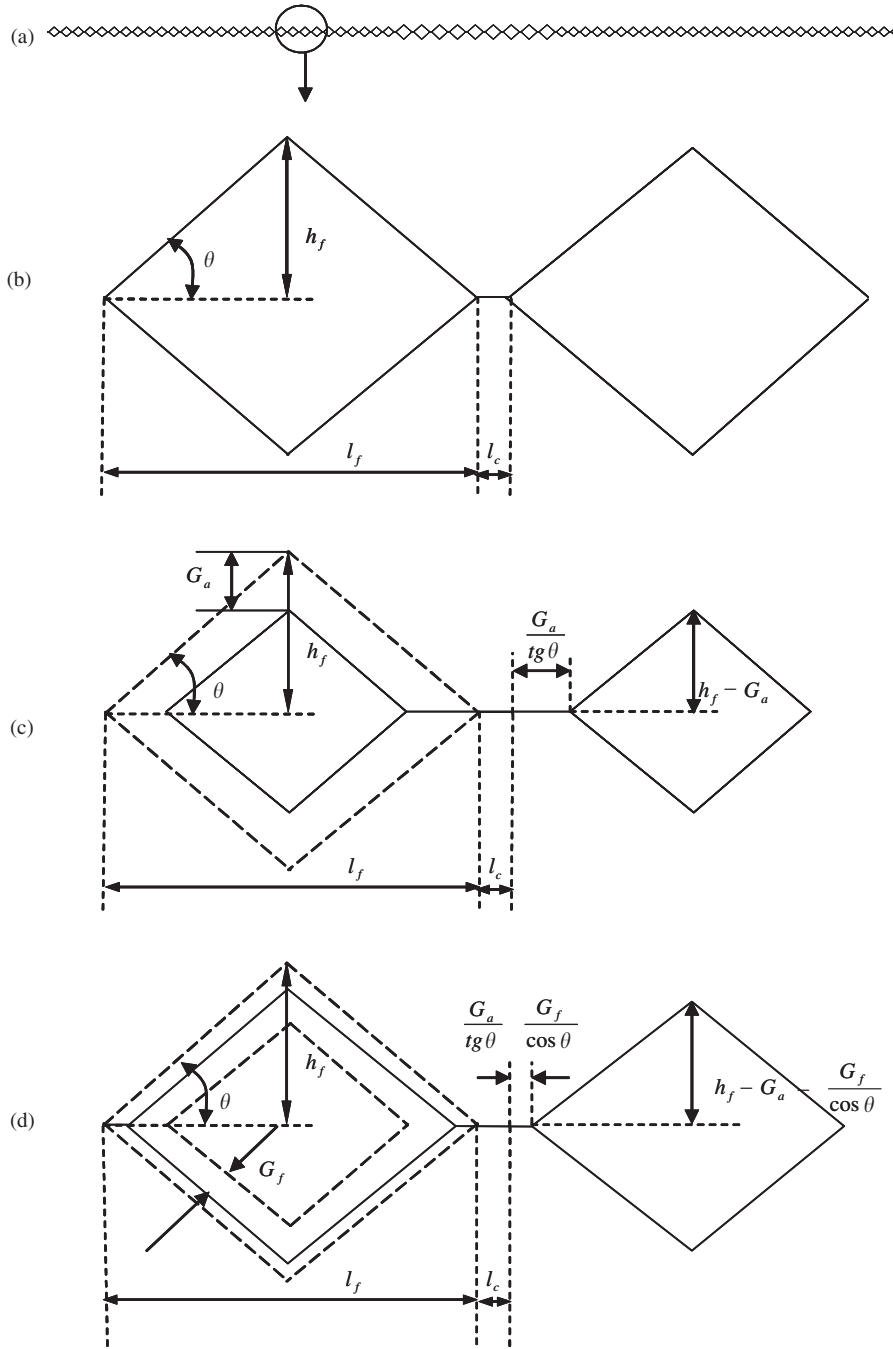


Fig. 6. Schematic of the rock fracture profile model and its evolution due to pressure dissolution and free-face dissolution: (a) fracture profile; (b) definition of a pore by four parameters; (c) modification of the pore due to pure pressure dissolution; and (d) modification of the pore due to pure free-face dissolution.

transitioning, the flow path remains unchanged. Therefore, dissolution will not alter the flow field. For the case of fracture sealing or opening, the flow path becomes smaller or larger. Therefore, dissolution will alter the flow field. Subsequently, the differential pressure can increase or decrease if the flow rate in the flow path is a constant. With the non-uniform fracture geometry, preferential flow paths may form under mixed dissolution situation.

3.4. Fully coupled HMC model

3.4.1. Initial fracture model

As shown in Fig. 6(a), to simulate the initial non-uniform distribution of fracture geometry, the fracture profile is simplified to be represented by two different pore size populations, l_{f1} and l_{f2} , h_{f1} and h_{f2} , with identical pore-wall inclinations, θ . This selection is based on observations that the small-sized pores flank a

central zone of the fracture containing larger pores. The ratio of the width of the total of the small pores to the diameter of the sample, r_{l1} , is defined as $r_{l1} = W_1/W$, where W_1 is the width of the total of the small pores and W is the diameter of the sample. Geometric parameters, h_{f1} , l_{f1} , l_{c1} , represent the small-sized pores, while h_{f2} , l_{f2} , l_{c2} , the large-sized pores. It is assumed that

$$r_h = \frac{h_{f2}}{h_{f1}} = \frac{l_{f2}}{l_{f1}} = \frac{l_{c2}}{l_{c1}}. \quad (12)$$

Under this condition, the ratio of contact areas is defined as

$$r_a = \frac{l_{c1}}{l_1} r_{l1} + \frac{l_{c1}}{l_1} (1 - r_{l1}). \quad (13)$$

3.4.2. Flow in the fracture

The fluid flux through a single constant section triangular-pore (as illustrated in Fig. 6b) under the differential pressure, ΔP , can be defined as

$$q = 2 \frac{\Delta P}{12\mu L} \int_0^{(h_f/\tan\theta)} (2x \tan\theta)^3 dx = \frac{4}{\tan\theta} h_f^4 \frac{\Delta P}{12\mu L}, \quad (14)$$

where μ is temperature-dependent dynamic viscosity of the fluid ($\text{ML}^{-1}\text{T}^{-1}$), L is length of the sample (L), q is flow rate (L^3T^{-1}), and ΔP is the differential pressure ($\text{MT}^{-2}\text{L}^{-1}$). Eq. (14) implies an assumption that the cubic law of fracture comes into existence at each dx . This is the lubrication approximation. Different methods to estimate the hydraulic conductance for laminar flow through irregularly shaped tubular pores can be found in Sisavath et al. [50].

The number of i -sized pores per fracture width W is defined as

$$n_i = \frac{W}{l_i} = \frac{W}{(2h_{fi}/\tan\theta) + l_{ci}} \quad (i = 1, 2). \quad (15)$$

Therefore, the fluid flowrate in fracture width W with i -sized pores can be defined as

$$q_i = q n_i = (2h_{fi})^3 \frac{h_{fi}}{2l_i \tan\theta} \frac{\Delta P W}{12\mu L}. \quad (16)$$

The flowrate through all small-sized pores is calculated as

$$Q_1 = q_1 r_{l1} = (2h_{f1})^3 \frac{h_{f1}}{2l_1 \tan\theta} r_{l1} \frac{\Delta P W}{12\mu L}. \quad (17)$$

The flowrate through all large-sized pores is calculated as

$$Q_2 = (2h_{f2})^3 \frac{h_{f2}}{2l_2 \tan\theta} (1 - r_{l1}) \frac{\Delta P W}{12\mu L}. \quad (18)$$

The flowrate expressed with the equivalent hydraulic aperture is

$$Q = \frac{\Delta P W}{12\mu L} \bar{b}^3, \quad (19)$$

where \bar{b} is the equivalent hydraulic aperture of rock fracture. Total flowrate is the sum of all components, as

$$Q = Q_1 + Q_2 \quad (20)$$

and with substitution of Eqs. (17) through (18) into (20) gives

$$\frac{4h_{f1}^4 W r_{l1}}{l_1 \tan\theta} + \frac{4h_{f2}^4 W (1 - r_{l1})}{l_2 \tan\theta} = \bar{b}^3 W, \quad (21)$$

where

$$h_{f1} = h_{f1}|_{t=0} - \left(G_a - \frac{G_f}{\cos\theta} \right), \quad (22)$$

$$h_{f2} = r_h h_{f1}|_{t=0} - \left(G_a - \frac{G_f}{\cos\theta} \right), \quad (23)$$

where t is time. Note that all geometric parameters of fracture are functions of time.

From Eq. (21), the initial height of the small-sized pore, h_{f1} at $t = 0$ s, can be obtained from

$$h_{f1}|_{t=0} = \frac{\bar{b}|_{t=0}}{2} \sqrt[3]{4 \frac{l_1|_{t=0}}{2h_{f1}|_{t=0}/\tan\theta r_{l1}|_{t=0} + (1 - r_{l1}|_{t=0})r_h^3|_{t=0}}}. \quad (24)$$

3.4.3. Mass balance

With Eqs. (6) and (7), the removed mineral volume from one i -sized pore and its tributary contact area can be calculated as

$$\Delta V_{\text{removi}} = 2 \left(\left(l_{ci} + \frac{G_a}{\tan\theta} \right) G_a + \left(\frac{h_{fi}}{\sin\theta} + \frac{G_f}{\tan\theta} \right) 2G_f - 2G_a \frac{G_f}{\sin\theta} \right) \quad (i = 1, 2). \quad (25)$$

Then the total volume removed from the fracture surface, V_{remov} , is

$$V_{\text{remov}} = [\Delta V_{\text{remov1}} n_1 r_{l1} + \Delta V_{\text{remov2}} n_2 (1 - r_{l1})] W L, \quad (26)$$

where ΔV_{remov1} is the volume removed from one small pore and its tributary contact area, and ΔV_{remov2} is the volume removed from one large pore and its tributary contact area. Eqs. (25) and (26) are used to calculate the mass removed during dissolution.

3.4.4. Determination of effective stress

As the fracture profile changes, the mass removal modified average effective stress can be solved through

the equilibrium relationship among the average effective stress at contact areas, σ_{eff} , the ambient confining stress of rock core, σ_{amb} , and the pore pressure, P , as

$$\sigma_{\text{amb}}W = \sigma_{\text{eff}}r_aW + P(1 - r_a)W. \quad (27)$$

Solving Eq. (27) gives

$$\sigma_{\text{eff}} = \frac{\sigma_{\text{amb}}}{r_a} - \frac{1 - r_a}{r_a}P, \quad (28)$$

where r_a is the ratio of contact areas of rock fracture and will changes with dissolution.

The critical stress, σ_c , in Eq. (2) may be evaluated from the enthalpy of fusion and the melting temperature of calcite, although it is difficult to constrain [46]. The critical stress is not equivalent to the uniaxial compressive strength, but may be physically related to it. The uniaxial compressive strength of limestone (intact rock) is typically in the range 10–100 MPa. For asperities on rock fracture surface, the value of critical stress, σ_c , should be smaller than that of intact rock. Our calculations are conducted with a critical stress, σ_c , of 6.65 MPa, which is defined as the stress when the average relative contact area in the whole fracture surface is about 50% [8]. This contact area rate is the eventual rate after removal of asperities by pressure dissolution. Montemagno and Pyrak-Nolte [33] measured void area in the individual fracture ranged between 45% and 58% with X-ray tomography.

3.4.5. Fully coupled equations

The above processes, including pressure dissolution, free-face dissolution, fluid flow in the fracture, and mass balance, are fully coupled, which are summarized as follows:

$$\frac{dG_a}{dt} = \alpha(\sigma_{\text{eff}} - \sigma_c)^\beta, \quad (29)$$

$$\frac{dG_f}{dt} = \gamma, \quad (30)$$

$$\frac{4h_{f1}^4Wr_{l1}}{l_1 \tan \theta} + \frac{4h_{f2}^4W(1 - r_{l1})}{l_2 \tan \theta} = \bar{b}^3W, \quad (31)$$

$$V_{\text{remov}} = [\Delta V_{\text{remov}1}n_1r_{l1} + \Delta V_{\text{remov}2}n_2(1 - r_{l1})]WL. \quad (32)$$

Eqs. (29) through (32) are fully coupled through the competing processes of pressure dissolution at asperity contacts and free-face dissolution at pore walls. The pressure dissolution and free-face dissolution alter fracture topography and flow topology. During each time step, Δt , the updated contact area, aperture, effective stress and fracture geometrical parameters are used in Eqs. (29) through (32).

4. Simulation of the experiment

4.1. Computational procedure

The individual processes of pressure solution at asperity contacts and free-face dissolution at pore walls are combined to define the progress of aperture reduction/increase of the fracture with time. In the initial condition, an initial fracture geometry (including geometric parameters of pores, h_{fi} , l_{fi} , l_{ci} , a small representative contact area, r_a , the inclination of the pore wall, θ , and the critical stress, σ_c , et al.) is set for calculation. The average effective stress on asperity contact areas can be calculated by Eq. (28) with applying ambient stress. With the initial fracture geometry, the total values of asperity height, G_a , by pressure solution, and retreat of pore wall, G_f , by free face dissolution at each stage are calculated by the flux equivalent principle applied in Eq. (31), the mineral mass balance Eq. (32), and geometric relations (29) and (30). Then, the values of α , β , and γ are determined numerically. During time step, Δt , appropriate magnitudes of mass dissolution at contact areas and free-face dissolution at pore walls are simultaneously evaluated from Eqs. (29) and (30), respectively. From the known magnitude of the diffusing mass, the updated contact area and aperture are calculated from Eqs. (7) and (6). Net dissolution from the pore wall (Eq. (30)) and resulting enlargement of the void cavity will compete with the closure occasioned by the shortening of the bridging asperity. The dominant process will prescribe whether the fracture gapes or seals. If the effective stress decreases to the critical stress, pressure solution ceases and only free-face dissolution exists.

In the above computational process, the equivalent hydraulic aperture, \bar{b} , differential pressure, ΔP , the effective stress at asperity contacts, σ_{eff} , and the total removed mineral volume, ΔV_{remov} at each time-step are calculated from Eqs. (18), (8) and (23), respectively.

4.2. Simulation results

An initial fracture geometry is set to initiate the calculation. The diameter (W) and the length (L) of the sample is 50 mm and 108 mm, respectively. It is assumed that the inclination of the pore wall is, $\theta = 30^\circ$, the ratio of pore size is, $r_h = 1.5$, and the critical stress is $\sigma_c = 6.65$ MPa, which is the effective stress while the average relative contact area is 52.6%. Many test data show that the permeability of rock fractures is insensitive to changes in stress when relative contact areas approach 40–70% [51]. The ratio of the width of the total of the small-sized pores to the diameter of the sample is assumed to be $r_{l1} = 0.8$. Percentage values of contact areas (r_a) of a gneiss joint as determined with CT for characteristic CT numbers of 1200 is 5.68–7.10%

under the conditions of normal stress, σ_n , of 0.11–0.22 MPa and tangential displacement of 2 mm [41]. In our calculation, the average ratio of contact areas, $r_a|_{t=0}$, is assumed to be 10% under the applied normal stress of 3.5 MPa. From Eq. (21), it can be calculated that $h_{f1} = 17.3 \mu\text{m}$, $h_{f2} = 26.0 \mu\text{m}$, $l_1 = 66.7 \mu\text{m}$, and $l_2 = 100.0 \mu\text{m}$. The initial geometrical parameters of fracture profile are summarized in Table 1.

Eq. (5) is used to calculate free-face dissolution instead of Eq. (4) in our numerical simulation. Throughout the test duration, calcium concentration and magnesium concentration within the fluid remain between 40–60 and 20–30 ppm, respectively. In an open system at 10 °C, dissolved calcite reaches equilibrium at $C_{\text{eq}}(C_a\text{CO}_3) \text{ equivalent} = 273 \text{ mg L}^{-1}$ [7]. The concentration within the fluid does not vary greatly during the test, so the variation of concentration does not unduly influence the retreat rate of the pore walls.

In the following numerical simulation, the complete experiment is divided into three stages: the first stage circulated by sampled groundwater, 0–932 h, and the second and third stages from 932 to 1071 h, and from 1071 to 1487 h, circulated by distilled water.

In the first stage of the experiment, circulated by groundwater (0–932 h), the magnitudes of the controlling constants are $\alpha = 0.018$, $\beta = 0.4$, and $\gamma = 0.030$. Asperities and the free-faces of the fracture are both net removed, simultaneously, but the influence of effective stress dominates the response. The local magnitude of the confining stress diminishes gradually from 35.0 to 11.9 MPa, as the ratio of contact areas increases.

In the second stage of the experiment, circulated by distilled water (932–1071 h), the magnitudes of the controlling constants are $\alpha = 0.049$, $\beta = 0.54$, and $\gamma = 0.012$. The removal of asperities accelerates because of the lower pH of the distilled water as permeant. As the relative contact area increases, the role of stress in mediating pressure solution diminishes quickly. At the end of this stage, the effect of stresses on dissolution almost disappears, and the average relative contact area increases above 50%. The small pores are almost closed, and the main fluid flow (above 80%) goes through the

large pores. For example, at 1071 h, $\sigma_{\text{eff}} = 6.745 \text{ Mpa}$, while the average relative contact area is 51.9%, and the effective stress is close to the critical stress, σ_c .

In the third stage of the experiment, still circulated by distilled water (1071–1487 h), the magnitudes of the controlling constants are $\alpha = 0.0$, $\beta = 0.0$, and $\gamma = 0.067$. The height of the small-sized pores is 8.69 μm at 1071 h, and there is only a small part of the flux (below 20%) that flows through the small pores—so it can be simply assumed that the small pores are closed completely (flow can take place only through the hydraulic aperture), and consequently all fluid flows through the large pores. Correspondingly, the effect of stress disappears completely so that only the free-face of the pore wall of the large pores is dissolved. In this stage, the rate of free-face dissolution (γ), is increased from 0.012 to 0.067 in the first 150 h of this stage, and then asymptotes to $\gamma = 0.067$ for the rest of the simulation. As the free surface dissolution within the large pores increases, the contact areas in the large pores disappear, the fracture opens and the wormhole forms gradually. At the end of this stage, the aperture of the wormhole is almost 100 μm (Fig. 11). The calculated geometric parameters for different simulation stages are summarized in Table 2.

In the first circulation of groundwater, the calculated removed volume is 360.7 mm^3 , which is consistent with the tested removed volume, 360 mm^3 . In the second circulation of distilled water, the calculated removed volume is 131.1 mm^3 , which is 81.9% of the tested removed volume, 160 mm^3 . The discrepancy could be because of the dissolution resulting from flow in the hydraulic apertures (Fig. 7).

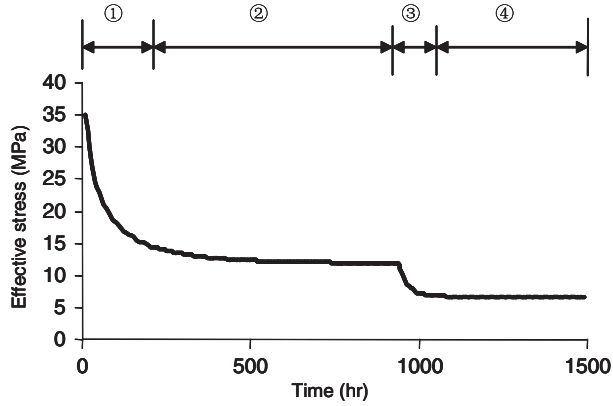
Comparisons of model results with experimental data are shown in Figs. 8–11. These results show a close correspondence between the representation for pressure-drop across the sample, that is in turn conditioned by the evolution of aperture represented by this diagnostic model. The results for mass removal rates are less congruent, especially in the early portion of the test where the small difference between inlet and outlet concentrations gives unreasonably large and variable rates (Fig. 10). This discrepancy stems mainly from experimental errors, predicting unreasonably large

Table 1
Initial geometrical parameters describing the fracture

Description	Value
Diameter of the sample W (mm)	50
Length of the sample L (mm)	108
Ratio of total width of small-sized pores to diameter of the sample r_{11}	0.8
Inclination of the pore wall θ (°)	30
Ratio of pore size r_h	1.5
Average ratio of contact areas r_a	0.1
Height of a small-sized pore h_{f1} (μm)	17.3
The critical stress σ_n (MPa)	6.65

Table 2
Calculated geometrical parameters for different simulation stages

T (h)	h_{f1} (μm)	l_{c1} (μm)	h_{f2} (μm)	l_{c2} (μm)
0	17.3	6.67	26.0	10.0
932	13.34	20.49	22.04	23.65
1071	8.69	36.60	17.39	39.76
1210	8.69	36.60	22.35	22.58
1350	8.69	36.60	35.38	0.0
1487	8.69	36.60	49.64	0.0



① Pressure dissolution dominates; ② A balance of pressure dissolution and free-face solution is almost achieved. ③ Pressure dissolution dominates; ④ Pressure dissolution ceases and only free-face dissolution occurs on large-sized pores.

Fig. 7. Evolution of average effective stress in the fracture. Based on the stress evolution, four different dissolution stages are recognized as pressure dissolution mode, mixed pressure and free-face dissolution mode; pressure dissolution mode; and free-face dissolution mode.

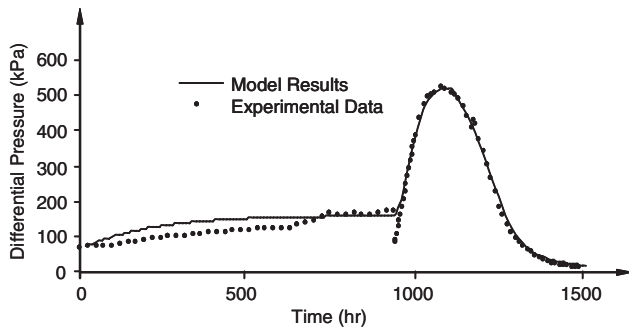


Fig. 8. Comparison of model results with experimental data: differential pressure vs. time.

magnitudes of mass removal, not confirmed by imaging results.

Changes in average effective stress during whole test process are shown in Fig. 7. In the first 150 h of the first circulation of groundwater, pressure dissolution dominates, and average aperture is reduced. Asperities are removed rapidly, and asperity contact areas increase, so the effective stress decreases very rapidly. From 150 to 932 h of the first circulation, the effective stress decreases gradually, a balance of pressure dissolution and free-face solution is almost achieved. Pressure dissolution dominates weakly and average aperture decreases slowly. But the effective stress remains above 12 MPa and the contact areas rate is about 29%.

In the first 140 h of the second circulation of distilled water, pressure dissolution dominates again because of the lower pH value of distilled water. The average aperture reduces rapidly to about 12 μm. The effective stress on the contact areas reduces to the critical stress, σ_c , and pressure solution ceases. The contact area

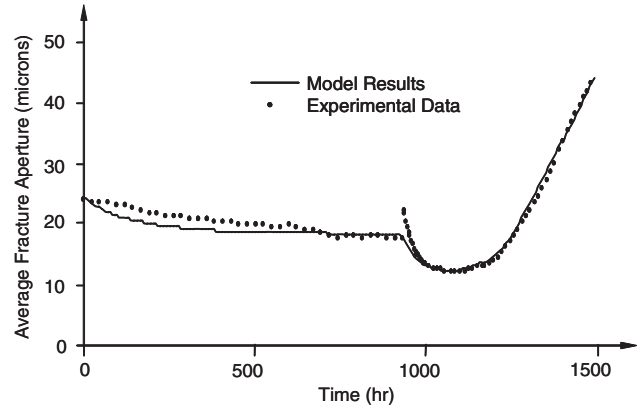


Fig. 9. Comparison of model results with experimental data: average fracture aperture vs. time.

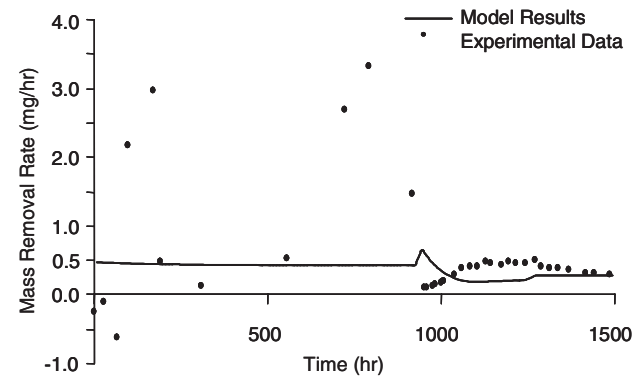


Fig. 10. Comparison of model results with experimental data: Mass Removal Rate vs. Time.

increases above 50%, and most smaller-sized pores become too small to connect each other, which are assumed to have no contribution to the permeability of the fracture. So from 1071 to 1487 h of the second circulation of distilled water, only free-face dissolution occurs in well-contacted larger-sized pores. The permeability of the fracture increases rapidly with the retreat of local larger-sized pore walls, and wormholes form in the locations of a few local larger-sized pores gradually by free-face dissolution.

5. Conclusions and discussions

A diagnostic dissolution-dependent model is developed and applied to explore the spontaneous switching of permeability changes in a limestone fracture with net dissolution, as reported in a companion paper [8]. In the model, dissolution mechanisms within the fracture switch from mixed-mode (a combination of pressure dissolution and free-face dissolution) to a single mode (pressure dissolution or free-face dissolution only), as conditioned by the twin outputs of dissolved mineral mass and measured pressure drop. This allows both the

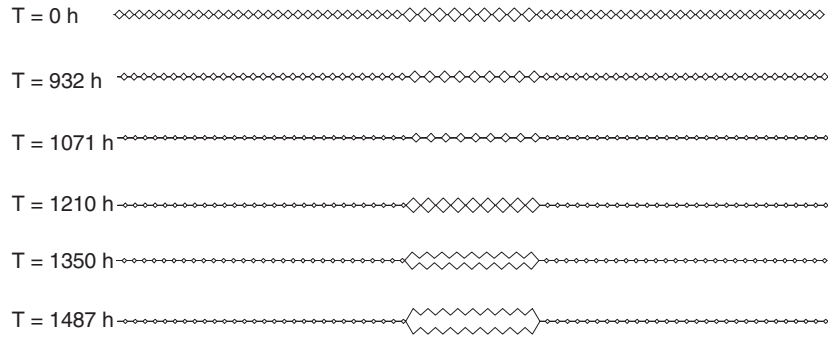


Fig. 11. Evolution of the simulated fracture aperture at different times.

permeability reduction as mineral mass is net removed from contacting asperities, and the permeability enhancement as free-face dissolution localizes along a solution channel, to be quantified, using consistent parameters over ranges of the experiment. Specifically, the values of parameters, α , β , and γ , determine the relative importance of each mode in defining the progress towards an ultimate porosity.

The flow of ground water in the first stage of the experiment caused the impedance to increase monotonically as contacting asperities were removed, and the fracture walls closed. These observations indicate that dissolution in the fracture is mixed-mode. Matching the simulation results with the experiment yields the parameters, α , β , and γ , as 0.030, 0.400 and 0.018, respectively, for the first part of the experiment (0–932 h).

The switch in permeant from ground water to distilled water caused accelerating changes in flow impedance; an initial rapid increase in impedance (closure in aperture), subsequently halted, and spontaneously transformed into an exponentially decreasing impedance, corresponding to the observed growth of a wormhole. The initial measured increase in impedance is consistent with closure of the fracture resulting from the fast removal of asperities from contact areas. These observations indicate that dissolution in the fracture is also in mixed mode, but pressure dissolution plays an increased role. Therefore, the value of γ should be smaller and the values of α and β should be larger than in the first stage of the experiment. Through matching the simulation results with the experimental data, the values of parameters, α , β , and γ , are determined numerically as 0.049, 0.540 and 0.012, respectively, for the second stage of the experiment (932–1071 h).

With continued circulation of distilled water at constant flow rate, the sample reaches the maximum impedance as the concentration of the effluent approaches a steady maximum of 5 ppm Ca. Following this, the impedance sharply drops with the observed development of a dominant flow channel. This occurs

Table 3
Values of α , β , γ for the three stages

	α	β	γ
Stage 1	0.018	0.40	0.030
Stage 2	0.049	0.54	0.012
Stage 3	0.0	0.0	0.067

with no changes in the other experimental conditions, or in the resulting concentration of the effluent, recording net removal of mass from the sample. These observations indicate that free-face dissolution dominates while the role of pressure solution diminishes. This is confirmed in that the evaluated values of α and β are null and the value of γ should be much higher than previous stages. Through matching the simulation results with the experimental data, the parameter, γ , is determined numerically as 0.067 for the third stage of the experiment (1071–1487 h).

Finally, some discussion of the alpha, beta, gamma coefficients in Eqs. (2) and (5) is given below. The values of α , β , γ for the three stages in the fitting procedure which are determined numerically are given in Table 3.

There are several relationships between dissolution and normal pressure that are suitable for systems involving grain-to-grain contacts, which may not be applied directly to fractures due to the existence of rock bridges (contact areas) instead of grain–grain contacts. In this paper, Eqs. (2) and (5) are assumed relations that represent the anticipated multi-mode response of the dissolution/precipitation process, driven by stresses. Many factors influence dissolution, such as stress, temperature, the pH value of circulated water, the physical properties of the fracture material, the geometrical distribution of the fracture surface, and time-dependent closure of a fracture under constant normal stress [52]. Currently, there is no exact physical expression involving the influence of the above physical factors on dissolution, so the value of α , β and γ are determined numerically.

We compared the fitted magnitudes of α and γ for the pressure dissolution within a limestone fracture to the ones estimated for the grain-to-grain pressure dissolution within the limestone matrix. As shown in Eq. (1), the magnitude of α_0 for the grain-to-grain dissolution can be defined as

$$\alpha_0 = \frac{3V_m^2 k_+}{RT}, \quad (33)$$

where V_m is the molar volume of the solid ($3.69 \times 10^{-5} \text{ m}^3 \text{ mol}^{-1}$ for calcite) [53], k_+ is the dissolution rate constant ($1.15 \times 10^{-6} \text{ mol m}^{-2} \text{ s}^{-1}$ for calcite) [53], R is the gas constant ($8.314 \text{ J mol}^{-1} \text{ K}^{-1}$), and T is the temperature (293.2 K or 20 °C). Substituting these numbers into Eq. (33) gives $\alpha_0 = 1.927 \times 10^{-18} \text{ mPa}^{-1} \text{ s}^{-1} = 1.927 \times 10^{-6} \text{ } \mu\text{m MPa}^{-1} \text{ s}^{-1}$. Apparently, this value is about 10000 times lower than the average fitted α in our model, which is $0.033 \text{ } \mu\text{m MPa}^{-1} \text{ s}^{-1}$. The average fitted magnitude for β is 0.47, which represents the unloading case where the ambient stress is applied at the beginning as discussed in 3.1. If $\beta = 1$, it represents the case for the grain-to-grain pressure dissolution. The higher value of α suggests that the pressure dissolution inside a limestone fracture might much faster than the grain-to-grain pressure dissolution inside the rock matrix, and the non-unity value of β suggests that the relation between the pressure dissolution rate and the stress difference inside the fracture is nonlinear. Those phenomenal observations demonstrate that the mechanism of pressure dissolution inside a rock fracture may be significantly different from that within rock matrixes. This difference will be thoroughly investigated in our future research.

For free-face dissolution, the fitted magnitudes for γ are 0.03 for the first 932 h experiment and 0.067 for the last 416 h experiment, respectively. According to the aquatic chemistry [54], $\gamma = 0.03$ corresponds to the dissolution rate of $4.2 \times 10^{-11} \text{ mol m}^{-2} \text{ s}^{-1}$ for CaCO_3 , and $\gamma = 0.067$ corresponds to the dissolution rate of $8.8 \times 10^{-11} \text{ mol m}^{-2} \text{ s}^{-1}$ for CaCO_3 . These numbers are within the same order of magnitude as the experimental dissolution rate, which is about $10^{-10} \text{ mol m}^{-2} \text{ s}^{-1}$ at $\text{PH} = 7$ [54]. This suggests that the free-face dissolution rate numerically fitted in this study is consistent with the aquatic chemistry.

Acknowledgements

This work is a result of partial support under grants ARC-DP0209425 and DOE-BES-DE-FG02-00ER15111. This support is gratefully acknowledged. The authors also thank Ozgen Karacan for help in the CT-scanning and two anonymous reviewers for their constructive comments.

References

- [1] Tenthorey E, Cox SF, Todd HF. Evolution of strength recovery and permeability during fluid-rock reaction in experimental fault zones. *Earth Plane Sci Lett* 2003;206:161–72.
- [2] Moore DE, Lockner DA, Byerlee JD. Reduction of permeability in granite at elevated temperature. *Science* 1994;265:1558–61.
- [3] Lin W, Roberts J, Glassley W, Ruddle D. Fracture and matrix permeability at elevated temperatures, Workshop on Significant Issues and Available Data, Near-field/Altered Zone Coupled Effects Expert Elicitation Project, San Francisco, November; 1997.
- [4] Polak A, Grader A S, Wallach R, Nativ R. Chemical diffusion between a fracture and the surrounding matrix: measurement by computed tomography and modeling. *Water Resour Res* 2003;39(4):1106.
- [5] Durham WB, Bourcier WL, Burton EA. Direct observation of reactive flow in a single fracture. *Water Resour Res* 2001;37:1–12.
- [6] Liu X, Ormond A, Bartko K, Li Y, Ortoleva P. A geochemical reaction-transport simulator for matrix acidizing analysis and design. *J Petrol Sci Eng* 1997;17:181–96.
- [7] Palmer AN. Origin and morphology of limestone caves. *Geol Soc Am Bull* 1991;103:1–21.
- [8] Polak A, Elsworth D, Liu J, Grader A. Spontaneous switching of permeability changes in a limestone fracture with net dissolution. *Water Resour Res* 2004;40:W03502.
- [9] Sprunt ES, Nur A. Reduction of porosity by pressure solution: experimental verification. *Geology* 1976;4:463–6.
- [10] Renard F, Park A, Ortoleva P, Gratier J-P. An integrated model for transitional pressure solution in sandstones. *Tectonophysics* 1999;312:97–115.
- [11] Weyl PK. Pressure solution and the force of crystallization—a phenomenological theory. *J Geophys Res* 1959;64(11):2001–25.
- [12] Morrow CA, Moore DE, Lockner DA. Permeability reduction in granite under hydrothermal conditions. *J Geophys Res* 2001;106:30,551–60.
- [13] Green HW. “Pressure solution” creep: some causes and mechanisms. *J Geophys Res* 1984;89(B6):4313–8.
- [14] Gratier J-P, Renard F, Labaume P. How pressure solution creep and fracturing process interact in the upper crust to make it behave in both a brittle and viscous manner. *J Struct Geol* 1999;21:1189–97.
- [15] Revil A. Pervasive pressure-dissolution transfer: a poro-viscoplastic model. *Geophys Res Lett* 1999;26(2):255–8.
- [16] Dewers T, Ortoleva P. A coupled reaction/transport/mechanical model for intergranular pressure solution, stylolites, and different compaction and cementation in clean sandstones. *Geochim Cosmochim Acta* 1990;54:1609–25.
- [17] Bosworth W. Strain-induced preferential dissolution of Halite. *Tectonophysics* 1981;78:509–25.
- [18] Tada R, Siever R. Experimental knife-edge pressure solution of halite. *Geochim Cosmochim Acta* 1986;50:29–36.
- [19] Tada R, Maliva R, Siever R. A new mechanism for pressure solution in porous quartzose sandstone. *Geochim Cosmochim Acta* 1987;51:2295–301.
- [20] Golfier F, Bazin B, Zarcone C, Lernormand R, Lasseux D, Quintard M. Acidizing carbonate reservoirs: numerical modeling of wormhole propagation and comparison to experiments. SPE 68922, SPE European Formation Damage Conference, The Hague, Netherlands, 21–22 May 2001.
- [21] Fredd CN, Fogler HS. Optimum conditions for wormhole formation in carbonate porous media: influence of transport and reaction. SPE 56995. *SPE J* 1999;4(3):196–205.
- [22] Buijse MA. Mechanisms of wormholing in carbonate acidizing. SPE 37283, SPE International Symposium on Oilfield Chemistry, Houston (TX), February 18–21 1997.

- [23] Hill AD, Zhu D, Wang Y. The effect of wormholing on the fluid loss coefficient in acid fracturing. SPE 27403, the SPE International Symposium on Formation Damage Control, Lafayette, Louisiana, February 7–10 1994.
- [24] Daccord G, Lietard O, Lenormand R. Chemical dissolution of a porous medium by a reactive fluid—II: convection vs. reaction behavior diagram. *Chem Eng Sci* 1993;48:179–86.
- [25] Daccord G, Touboul E, Lenormand R. Carbonate acidizing: toward a quantitative model of the wormholing phenomenon. SPE 16887, SPE Annual Technical Conference and Exhibition, Dallas, TX, 1987.
- [26] Hoefner ML, Fogler HS. Pore evolution and channel formation during flow and reaction in porous media. *AIChE J* 1988; 34(1):45–54.
- [27] Eriksson N, Gupta A, Destouni G. Comparative analysis of laboratory and field tracer tests for investigating preferential flow and transport in mining waste rock. *J Hydrol* 1997; 194:143–63.
- [28] Pruess K. On water seepage and fast preferential flow in heterogeneous, unsaturated rock fractures. *J Contaminant Hydrol* 1998;30:333–62.
- [29] Morris C, Mooney SJ. A high-resolution system for the quantification of preferential flow in undisturbed soil using observations of tracers. *Geoderma* 2004;118:133–43.
- [30] Goodwin AK, O’Neil MA, Anderson WF. The use of X-ray computer tomography to investigate particulate interactions within opencast coal mine backfills. *Eng Geol* 2003;70:331–41.
- [31] Karacan CO. An effective method for resolving spatial distribution of adsorption kinetics in heterogeneous porous media: application for carbon dioxide sequestration in coal. *Chem Eng Sci* 2003;58:4681–93.
- [32] Wildenschild D, Hopmans JW, Vaz CMP, Rivers ML, Rikard D, Christensen BSB. Using X-ray computed tomography in hydrology: systems, resolutions, and limitations. *J Hydrol* 2002;267:285–97.
- [33] Montemagno CD, Pyrak-Nolte LJ. Fracture network versus single fractures: measurement of fracture geometry with X-ray tomography. *Phys Chem Earth (A)* 1999;24(7):575–9.
- [34] Van Geet M, Swennen R, David P. Quantitative coal characterization by means of microfocus X-ray computer tomography, colour image analysis and back-scattered scanning electron microscopy. *Int J Coal Geol* 2001;46:11–25.
- [35] Mogensen K, Stenby EH, Zhou D. Studies of waterflooding in low-permeable chalk by use of X-ray CT scanning. *J Petrol Sci Tech* 2001;32:1–10.
- [36] Tidwell VC, Meigs LC, Christian-Freear T, Boney CM. Effects of spatially heterogeneous porosity on matrix diffusion as investigated by X-ray absorption imaging. *J Contam Hydrol* 2000;42:285–302.
- [37] Nakashima Y. The use of X-ray CT to measure diffusion coefficients of heavy ions in water-saturated porous media. *Eng Geol* 2000;56:11–7.
- [38] Ketcham RA, Carlson WD. Acquisition, optimization and interpretation of X-ray computed tomographic imagery: applications to the geosciences. *Comput Geosci* 2001;27:381–400.
- [39] Withjack EM, Durham JR. Characterization and saturation determination of reservoir metagraywacke from the Geysers corehole SB-15-D (USA), using Nuclear Magnetic Resonance Spectrometry and X-ray Computed Tomography. *Geothermics* 2001;30:255–68.
- [40] Schembre JM, Kovscek AR. A technique for measuring two-phase relative permeability in porous media via X-ray CT measurements. *J Petrol Sci Tech* 2003;39:159–74.
- [41] Re F, Scavia C. Determination of contact areas in rock joints by X-ray computer tomography. *Int J Rock Mech Min Sci* 1999;36:883–90.
- [42] Karacan CO, Mitchell GD. Behavior and effect of different coal microlithotypes during gas transport for carbon dioxide sequestration into coal seams. *Int J Coal Geol* 2003;53:201–17.
- [43] Karacan CO, Okandan E. Adsorption and gas transport in coal microstructure: investigation and evaluation by quantitative X-ray CT imaging. *Fuel* 2001;80:509–20.
- [44] Hirono T, Takahashi M, Nakashima S. In situ visualization of fluid flow image within deformed rock by X-ray CT. *Eng Geol* 2003;70:37–46.
- [45] Heidug W, Lehner FK. Thermodynamics of coherent phase transformations in nonhydrostatically stressed. *PAGEOPH* 1985;123:91–8.
- [46] Yasuhara H, Elsworth D, Polak A. The evolution of permeability in a natural fracture: the significant role of pressure solution. *J Geophys Res* 2004;109:B03204.
- [47] Yasuhara H, Elsworth D, Polak A. A mechanistic model for compaction of granular aggregates moderated by pressure solution. *J Geophys Res* 2003;108(B11):2530.
- [48] Dreybrodt W, Buhmann D. A mass transfer model for dissolution and precipitation of calcite from solutions in turbulent motion. *Chem Geol* 1991;90:107–22.
- [49] Dreybrodt W. Processes in karst systems. Springer series in physical environment. Heidelberg: Springer; 1988 288pp.
- [50] Sisavath S, Jing XD, Zimmerman RW. Laminar flow through irregularly shaped pore in sedimentary rocks. *Transp Porous Media* 2001;45:41–62.
- [51] Sheng J. Three-dimensional numerical studies toward coupled fluid flow and stress of jointed rock masses and its engineering application. Ph.D. thesis, Hohai University, Nanjing, 2000 [in Chinese].
- [52] Matsuki K, Wang EQ, Sakaguchi K, Okumura K. Time-dependent closure of a fracture with rough surface under constant normal stress. *Int J Rock Mech Min Sci* 2001;38:607–19.
- [53] Yasuhara H, Elsworth D, Polak A, Liu J, Grader A, Halleck P. Spontaneous permeability switching in fractures in carbonate: lumped parameter representation of mechanically and chemically mediated dissolution (Under review).
- [54] Stumm W, Morgan JJ. Aquatic chemistry: chemical equilibria and rates in natural waters. 3rd ed. New York: Wiley; 1996. p. 789.